Research Square

Preprints are preliminary reports that have not undergone peer review.
They should not be considered conclusive, used to inform clinical practice,
or referenced by the media as validated information.

# The Syncytial Mesh Model: glial spatial control, neuronal response geometry, and the limits of local EEG reduction

**Andreu Ballús Santacana**

andreu.ballus@uab.cat

Universitat Autònoma de Barcelona

**Research Article**

**Keywords:** astrocytes, spatial potassium buffering, neuronal-glial coupling, neural mass models, spatial modes, identifiability

**Posted Date:** October 27th, 2026

**DOI:** https://doi.org/10.21203/rs.3.rs-11421911/v1

**License:** This work is licensed under a Creative Commons Attribution 4.0 International License.
Read Full License

**Additional Declarations:** No competing interests reported.

# The Syncytial Mesh Model: glial spatial control, neuronal response geometry, and the limits of local EEG reduction

**Short title:** Spatial glial control in the Syncytial Mesh Model

Andreu Ballús Santacana
Department of Philosophy, Universitat Autònoma de Barcelona
Cerdanyola del Vallès, Spain
Corresponding author: andreu.ballus@uab.cat

## Statements and Declarations

Funding. No funding was received for this research.

Competing interests. The author declares no relevant financial or non-financial competing interests.

Author contributions. A.B.S. contributed to conceptualization, methodology, formal analysis, investigation, visualization, writing the original draft, and reviewing and editing the manuscript. A.B.S. reviewed and approved the final manuscript and accepts full responsibility for its content.

Data and code availability. The full availability statement is provided in the manuscript and the reproducibility archive is supplied as Online Resource 3.

Ethics approval and consent. This is a secondary analysis of publicly available, de-identified EEG. Original-study ethics and consent information is cited in the manuscript.

Related publications and preprints. Earlier SMM preprints and the separate published conceptual precursor are disclosed in the manuscript, cover letter, and Online Resource 2.

**Abstract**

Neuronal circuits generate most measurable electrophysiological currents, but slower physiological variables governing their excitability and spatial coordination need not be neuronal. The Syncytial Mesh Model (SMM) proposes that local astroglial coupling forms a distinct control geometry alongside neuronal connectivity. We formalize this architecture and examine a potassium-mediated realization (SMM-K). Under stated conditions its passive two-compartment ionic subsystem is dissipative. Coupled bidirectionally to neuronal populations, glial transport modifies responses to patterned perturbations. In a reproducible seven-domain linearized model, enabling reference transport reduces the central excitatory response by 24%, increases the adjacent response by 68%, and changes the adjacent-to-central ratio from 0.116 to 0.256 after 20 s of normalized focal glial input; homogeneous uniform forcing is transport-insensitive. The effect persists for focal neuron-derived potassium input with lateral neuronal coupling, but becomes small relative to neuronal propagation under direct neuronal excitation. A spatial-mode transfer function isolates the frequency-dependent transport sensitivity. The EEG predictor used in the frozen human comparison, however, retained only a local two-pole ionic filter and omitted spatial glial transport, making its predicted spectra exactly independent of the defining transport parameter. A separately documented post-open amended analysis of 535 participants favored a flexible generic two-state comparator over this local predictor (mean held-out difference -0.00918; 95% bootstrap interval [-0.01016, -0.00823]); the untouched primary remained not evaluable. SMM-K therefore yields a conditional spatial-intervention prediction, while the adverse EEG comparison constrains a narrower local projection rather than directly testing syncytial transport.

Keywords: astrocytes; spatial potassium buffering; neuronal-glial coupling; neural mass models; spatial modes; identifiability

## 1 Introduction

Macroscopic electrophysiological recordings primarily reflect neuronal transmembrane currents, but the physiological variables regulating neuronal excitability and spatial coordination need not themselves be neuronal. Oscillations, traveling waves, state transitions and intermittent coherence depend on local circuit dynamics, long-range structural connectivity and slower physiological processes. Astrocytes participate in extracellular ionic regulation, metabolic exchange, neuromodulatory responses and cortical state changes. Experimental manipulations show that astrocyte activity can influence transitions toward slow-oscillation states, while connexin-mediated astroglial networks contribute to sleep–wake regulation (Clasadonte et al. 2017; Poskanzer and Yuste 2016). Neuron–ion–glia models (Cressman et al. 2009; Halnes et al. 2013; Sætra et al. 2021; Sætra et al. 2023; Ullah et al. 2009) and coupled neuronal–astrocytic network models (Ali et al. 2025; Amiri et al. 2012; Gong et al. 2024; Lenk et al. 2020) establish the relevant biological and computational precedents.

Spatial potassium buffering is an established astroglial process. The recordings of Orkand, Nicholls and Kuffler (1966) and the synthesis by Kofuji and Newman (2004) established its physiological background. Connexin-deficient hippocampal preparations show that astrocytic gap-junction coupling contributes to potassium clearance and redistribution (Wallraff et al. 2006), while broader astroglial network manipulations affect extracellular potassium and glutamate handling, extracellular-space volume and synaptic physiology (Pannasch et al. 2011). These studies provide mechanistic precedents and experimentally accessible, though not perfectly selective, manipulations. The question addressed here is how the geometry of glial

transport changes neuronal responses, how stimulus pattern and frequency condition its visibility, and whether those dependencies survive an EEG observation reduction.

A distinct question is whether the spatial organization of glial networks changes neuronal responses in ways that cannot be captured by local glial feedback alone. The Syncytial Mesh Model (SMM) formalizes this possibility by separating neuronal current-generating states, long-range neuronal connectivity and locally coupled glial physiological states. This architecture is motivated by the three-layer and glial-control-field proposals of Ballús (2024) and Ballús Santacana (2026). The analysis here specifies a potassium-mediated realization, establishes properties of its passive ionic subsystem, derives stimulus-dependent spatial sensitivities, and examines how these dependencies are represented in an EEG predictor.

The distinction between neuronal and glial spatial operators has testable consequences. With neuronal connectivity and local parameters held fixed, changes in glial transport can redistribute a response to a spatially patterned input. A spatially local observation model may discard that transport dependence even when it is present in the underlying dynamics. Consequently, mechanistic inference requires explicit specification of the intervention, dynamical system and observation map; a good spectral fit or a failed local fit cannot independently determine the existence of spatial glial transport.

This is an important issue for electrophysiology. Neural-mass models and dynamic causal models fitted to power spectra or cross-spectral densities have an extensive history (Moran et al. 2007; Moran et al. 2009), as do spatial neural-field accounts of spectral modes (Robinson et al. 2001). Flexible periodic–aperiodic decompositions supply additional descriptive baselines (Donoghue et al. 2020). An EEG spectral fit is consequently not direct evidence that the latent timescale in the fitted model has a uniquely glial origin. Biological identification requires either

restrictions that preserve distinctive physiological commitments or observations that measure them independently.

The study addresses three questions. First, what causal architecture distinguishes glial-local transport from neuronal connectivity in a measurable dynamical model? Second, does a parameterized potassium realization predict a spatial neuronal response that depends on glial transport and stimulus geometry? Third, what does the human EEG comparison constrain when the implemented observation model retains local ionic feedback but omits spatial glial transport? The results combine analytical and numerical modeling with a non-confirmatory analysis of publicly available EEG; no new human intervention is reported.

## 2 Results

### 2.1 SMM is a coupled causal architecture, not an additional EEG source

The three-layer arrangement is shown in Fig. 1. Neuronal populations generate local electrical currents. Neuronal connections coordinate these currents across anatomical regions. The syncytial layer consists of physiological states distributed across a *different*, predominantly local glial transport or coupling geometry. This third layer is not an alternative connectome or an assertion that astrocyte calcium waves directly emit scalp EEG; it changes the excitability, effective gain, synaptic integration or stability of the neuronal system. If those changes persist long enough, they can alter the observable organization of low-frequency neuronal activity (Ballús Santacana 2026).

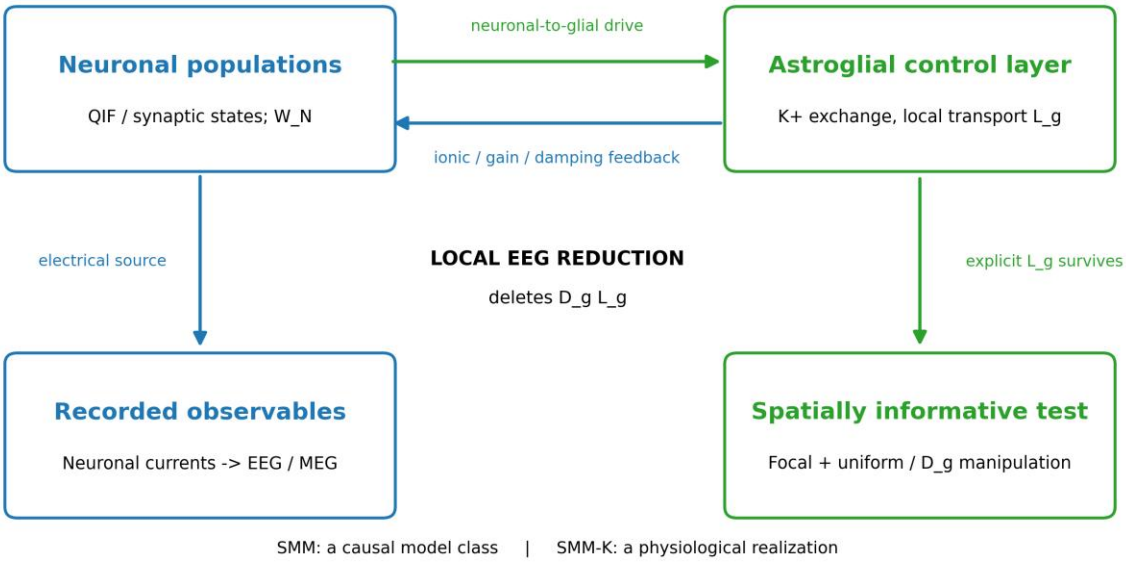


**Fig. 1** The SMM control architecture and the distinct observation paths

A class representative is

$$\dot{x} = F_N\big(x, W_N; \theta_N + \mathcal{C}(z)\big) + B_N u_N + \xi_N,$$
$$M_g \dot{z} = f_g\big(z, \mathcal{B}(x); \theta_g\big) - \mathcal{D}_g\big(L_g\big)z + B_g u_g + \xi_g,$$
$$y = H_N(x) + \nu.$$

Here $x$ denotes neuronal state variables, $W_N$ anatomical neuronal coupling, $z$ glial/extracellular physiological control variables, and $L_g$ a glial-local spatial operator. $H_N$ records neuronal rather than assumed direct glial electrical sources. A specific realization must specify the identities of $z$ and $\mathcal{C}$, the glial-to-neuronal and neuronal-to-glial feedback pathways, a regime in which the effective glial dynamics are slow, and an experiment for which $L_g$ matters to neuronal response while $W_N$ remains fixed. Spatial sensitivity is a causal requirement, not a requirement that every non-invasive recording detect it.

The same causal architecture can accommodate other physiological channels, including synaptic-gain and metaplastic, metabolic–neurovascular, and neuromodulatory processes (Ballús Santacana 2026). Those alternatives are not numerically validated by the potassium calculations

below. An effective damped-field equation represents a different dynamical assumption from passive potassium clearance: a dissipative ionic block cannot itself sustain delta/theta oscillations without neuronal feedback or additional active or restorative dynamics. The possible wave-field realization and its limits are treated in Online Resource 5.

Neuronal phase reductions, damped glial fields and glia-dependent distributed plasticity are possible extensions of the causal model class. A second-order damped-wave field requires a restoring or active regenerative process that is not supplied by passive potassium clearance, while a glial plasticity law requires explicitly specified and identifiable coupling terms. The corresponding equations, dimensional restrictions and evidence boundaries are provided in Online Resource 5. The quantitative spatial prediction analyzed in this paper concerns the potassium-mediated SMM-K realization alone.

**2.2 A potassium realization has a stable spatially coupled ionic component**

The explicit SMM-K realization uses extracellular potassium deviation $k$ and an effective astroglial potassium-load deviation $a$, with compartment fractions $\phi_e, \phi_a > 0$. With $J_N(x)$ a firing-related ionic source and $L_e, L_g$ symmetric nonnegative spatial Laplacians,

$$\phi_e \dot{k} = J_N(x) - (\kappa_e + \kappa_N)k + \kappa_a a - D_e L_e k,$$
$$\phi_a \dot{a} = \kappa_e k - \kappa_a a - D_g L_g a.$$

The coupling $k \to E_K \to \eta_N \to x$ closes the physiological loop through the potassium reversal potential and neuronal excitability, while the source $J_N$ supplies the reverse path. The neuronal realization follows an eight-state local construction formed by a six-dimensional excitatory–inhibitory QIF-derived linear block and the two ionic states; its numerical transcription is preserved and executable in the supporting code. QIF population reductions provide a principled mathematical point of entry (Montbrió et al. 2015), not a proof that the present parameters uniquely describe human cortex.

The source-free ionic subsystem obeys a strict quadratic energy inequality. For positive exchange and clearance coefficients,

$$V = 1/2\,\phi_e\kappa_e \parallel k \parallel^2 + 1/2\,\phi_a\kappa_a \parallel a \parallel^2,$$
$$\dot{V} = -\parallel \kappa_e k - \kappa_a a \parallel^2 - \kappa_e\kappa_N \parallel k \parallel^2 - \kappa_e D_e k^{\mathsf{T}} L_e k - \kappa_a D_g a^{\mathsf{T}} L_g a < 0$$

for nonzero state, under the stated conditions. The result does not require $L_e$ and $L_g$ to commute. It proves exponential stability of the passive *ionic* linear system and excludes its intrinsic oscillatory eigenmodes in that regime. It does not establish stability of every fully coupled nonlinear circuit. Oscillatory neuronal–glial interactions, and the field-level resonome described by SMM, require the relevant dynamical coupling and operating conditions to be specified rather than assigned to a passive diffusion operator.

The eight-state local Jacobian used in the calculations has slow ionic-dominated closed-loop eigenvalues near $-0.11293$ and $-12.31164\ \mathrm{s}^{-1}$. The computed spectral crossings occur near a neuronal drive of 8.132639 without the tested feedback and 8.133056–8.133972 for three prescribed feedback densities. The crossing shifts are small (approximately 0.005–0.016% of the reference threshold). They show that this *particular* local near-equilibrium feedback barely displaces the specified spectral threshold; they do not establish a universal bound on astroglial influences under spatial perturbations or different operating points. They are spectral crossings, not full nonlinear Hopf nondegeneracy certificates.

**2.3 A focal intervention reveals what spatial glial transport adds**

The theory's most direct positive prediction concerns *where* neuronal excitability changes after a spatially structured glial input. The seven-patch linear model contains eight local states per domain (56 states), $150\ \mu$m interpatch spacing, extracellular diffusion $D_e = 9.55343 \times 10^{-10}\ \mathrm{m^2 s^{-1}}$ and astroglial diffusion $D_g = 3.71479 \times 10^{-10}\ \mathrm{m^2 s^{-1}}$. The same neuronal matrices, extracellular diffusion, source intensity and observation were used when comparing

$D_g = 0$ and $D_g > 0$; only the glial transport parameter was changed. The fixed input was applied to the central astroglial equation. Responses are linear perturbations in arbitrary input normalization, not experimentally estimated human firing rates.

At 20 s, the central excitatory response was 0.0270742 in the no-transport condition and 0.0205800 with glial transport, whereas the neighboring response increased from 0.0031480 to 0.0052739. Thus the central response fell by 24.0%, the adjacent response rose by 67.5%, and the adjacent/central ratio increased from 0.1163 to 0.2563 (a factor of 2.20). A numerical sweep at 0, 0.25, 0.5, 1 and 2 times the reference $D_g$ yielded ratios 0.1163, 0.1590, 0.1959, 0.2563 and 0.3423, respectively. This directional monotonicity is specific to the simulated regime, not a general law of astrocytes. All tested linearizations remained stable.

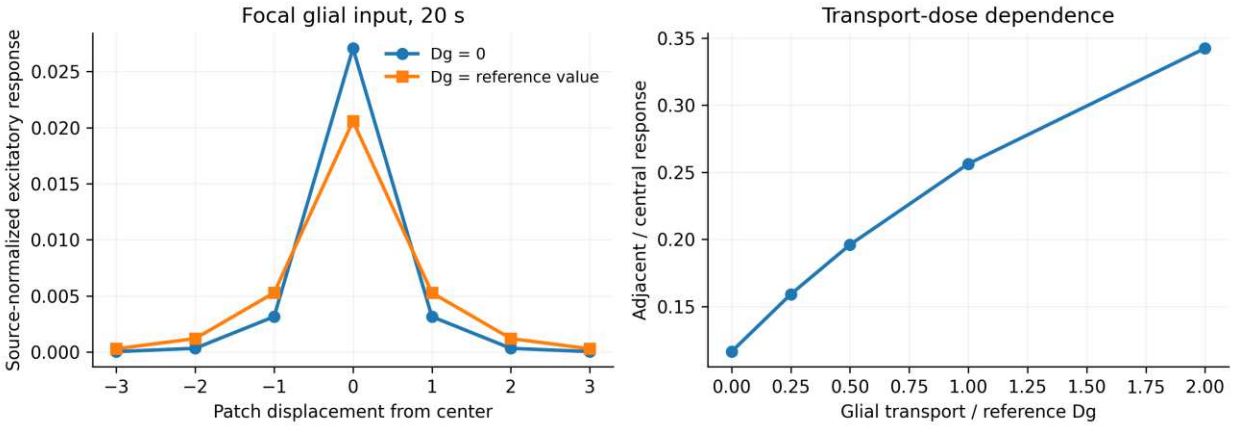


**Fig. 2** Neuronal spatial response and transport-dose discrimination in the seven-patch SMM-K realization

Under exactly uniform glial forcing in the homogeneous seven-patch model, the simulated difference between conditions was below $5.5 \times 10^{-15}$ at 20 s. This is the expected Laplacian result $L_g\mathbf{1} = 0$: a uniform glial input does not populate a transport-sensitive spatial mode. A purely uniform observation thus fails to test a parameter that changes a focal response. The biologically informative quantity is not an arbitrary change in global EEG power but the

interaction between the spatial pattern of a perturbation and neuronal response geometry. Figure 2 captures this result without asserting that a selective astroglial manipulation of equivalent strength has already been achieved experimentally.

**2.4 The focal prediction survives neuron-derived input and lateral neuronal coupling**

Direct astroglial-state perturbation is an idealized input. Two further forcing routes were evaluated with the same local eight-state Jacobian: a focal potassium-release source in the extracellular potassium equation and a focal excitatory-voltage drive that recruits the model's neuronal-rate-to-potassium feedback. For neuron-derived $K^+$ source input, the 20-s adjacent/central excitatory response ratio changed from 0.1180 at $D_g = 0$ to 0.2287 at the reference $D_g$; the center decreased from 0.027276 to 0.021733 while its adjacent patch increased from 0.003219 to 0.004970. Direct neuronal excitation also produced a nonzero but smaller transport-specific spatial response: its adjacent/central ratio changed from 0.000567 to 0.000876 in the uncoupled-patch calculation. The source-normalized drives are not calibrated to equal physiological doses, so only transport-on versus transport-off comparisons *within the same input route* are interpretable; the amplitudes are not absolute neuronal firing rates or empirical effect sizes.

A nearest-neighbor neuronal rate-coupling term was introduced $-\gamma_N L r_E$ to the same seven-patch system and varied $\gamma_N$ between 0 and 30 $s^{-1}$, always holding neuronal coupling constant between $D_g = 0$ and $D_g > 0$. With the focal neuronal $K^+$ source and $\gamma_N = 10$ $s^{-1}$, the adjacent/central ratio increased from 0.1333 to 0.2434 as glial transport was switched on. At $\gamma_N = 30$ $s^{-1}$ the corresponding ratios were 0.1612 and 0.2700. For focal neuron-derived $K^+$ input, the adjacent response increased by 54.4%, 45.9% and 34.8% at $\gamma_N = 0$, 10 and 30 $s^{-1}$, respectively, when glial transport was enabled; hence the transport effect remained substantial

throughout the tested stable lateral-coupling range. Direct focal excitatory drive behaved differently: with $\gamma_N = 10$ s$^{-1}$ its adjacent/central ratio changed only from 0.016153 to 0.016442, and at $\gamma_N = 30$ s$^{-1}$ from 0.044657 to 0.044913 (about 1.8% and 0.57% relative changes). At the latter coupling, glial transport changed the neighboring excitatory response by $1.32 \times 10^{-4}$, approximately 0.49% of the no-transport neighboring response. This small incremental effect was not erased mathematically, but neuronal spread dominated the ratio; detectability in biological tissue is unestablished. A second sensitivity check coupling neighboring excitatory rates into the excitatory-voltage equation retained the sign of the transport effect in the finite stable cases tested, not a similarly large effect size. Uniform-input $D_g$ sensitivity remained zero to numerical precision in all homogeneous variants. Full equations, sweep tables and a plotted comparison are given in Online Resource 6 and Online Resource 7; these retrospective sensitivity calculations were performed after the EEG outcome and neither constitute additional human tests nor exclude a suitably flexible neuronal-only spatial model.

**2.5 Spatial-mode analysis gives an explicit frequency-resolved discriminator**

The same prediction follows analytically for any spatial mode common to the two transport operators. With mode eigenvalues $\mu_e, \mu_g \geq 0$, introduce

$$\alpha_\mu = \frac{\kappa_e + \kappa_N + D_e\mu_e}{\phi_e}, \qquad \beta_\mu = \frac{\kappa_a + D_g\mu_g}{\phi_a}, \qquad \chi = \frac{\kappa_a\kappa_e}{\phi_e\phi_a}.$$

The linear transfer from neuronal potassium-source drive to extracellular potassium in that mode is

$$H_K(s;\mu_e,\mu_g,D_g) = \frac{s+\beta_\mu}{\phi_e\left((s+\alpha_\mu)(s+\beta_\mu)-\chi\right)}.$$

It follows, with neuronal and extracellular operators fixed, that

$$\frac{\partial H_K}{\partial D_g} = -\frac{\mu_g \chi}{\phi_e \phi_a \left((s+\alpha_\mu)(s+\beta_\mu) - \chi\right)^2}.$$

For $\mu_g = 0$, the sensitivity is exactly zero. For a nonuniform glial mode with $\mu_g > 0$, positive bidirectional exchange gives a nonzero transfer sensitivity away from poles. Thus, in a matched family with a *single spatial-mode-independent local filter* and otherwise fixed neuronal/extracellular operators, one cannot generally reproduce both the uniform and nonuniform transfer functions generated by changing $D_g$. The statement is explicitly conditional: sufficiently flexible models with alternative spatial couplings, neuronal propagation or additional latent states can mimic some observed effects. A compelling biological test must control or separately constrain those alternatives.

For the path geometry examined here, the relative difference $\left|H_K(D_g) - H_K(0)\right| / |H_K(0)|$ in the highest sampled nonuniform mode is about 0.35 at 0.018 Hz, 0.15 at 0.1 Hz, 0.0033 at 1 Hz and $1.2 \times 10^{-7}$ at 40 Hz. These are transfer-function sensitivities for the *ionic subsystem*, not estimates of human scalp EEG signal differences. Their frequency dependence follows from the actual coefficients. The analytical derivative was verified by numerical differentiation in the supplied script. The result motivates infraslow and local perturbation measurements but does not imply that every infraslow signal is glial.

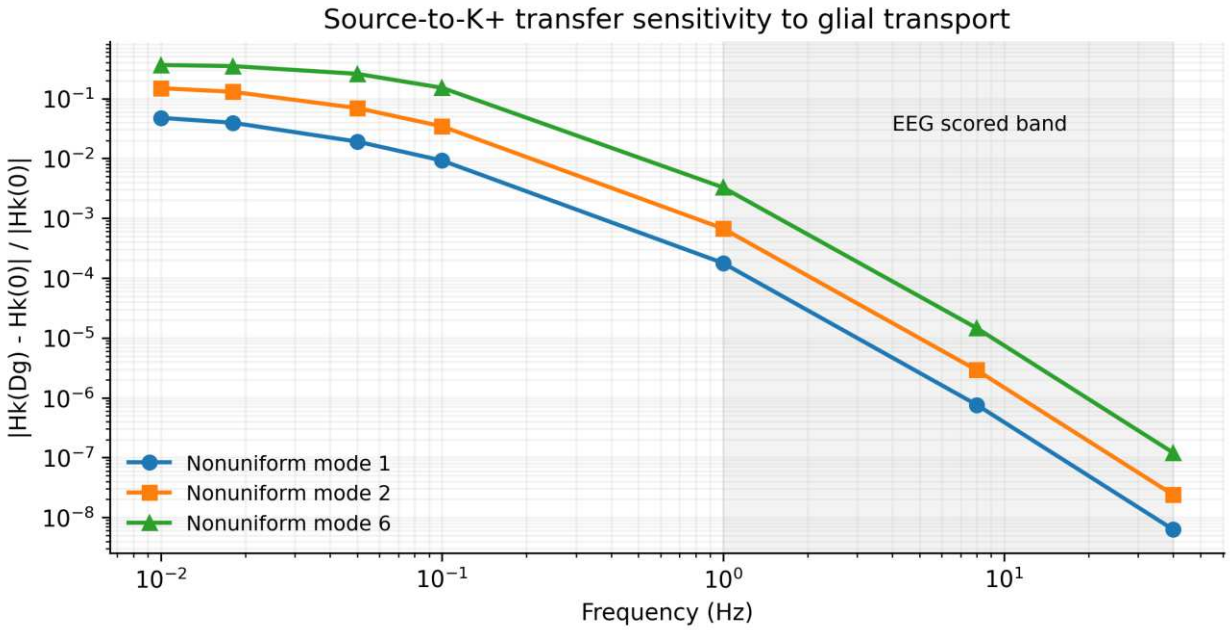


**Fig. 3** Frequency-selective transport dependence of nonuniform potassium modes; the frozen EEG analysis band is shaded

### 2.6 Local EEG reduction removes the parameter that differentiates SMM-K

The whole-brain EEG program used in the frozen comparison did not implement Eq (2) over the glial spatial graph. It retained the uniform-mode two-state $K$ transfer but used delayed neuronal regional connectivity $W_N$ and a template leadfield for long-range propagation and sensing. The model therefore contained no $D_g$, $L_g$ or glia-to-glia interpatch transport parameter. Its spectral predictions satisfy the exact program-level identity

$$\frac{\partial S_{\mathrm{EEG},M3}(f)}{\partial D_g} = 0 \quad \text{for all implemented frequencies } f,$$

when the fitted effective local constants are held fixed. This is structural absence, not an uncertain estimate. The frozen M3 was a *local potassium-mediated projection* of SMM-K, not its full spatial realization. The absence of glial transport arose at model construction, before test-score inspection; the subsequent equation-to-code analysis did not retrospectively alter the frozen predictor.

The implemented local filter has two isolated real poles, approximately $-12.32001$ and $-0.113735\ \mathrm{s}^{-1}$, and hence decomposes into two stable first-order filters. Its slow time constant is about 8.792 s and its corresponding corner frequency approximately 0.0181 Hz; the relevant *closed-loop* slow eigenvalue has a distinct 8.855 s time constant. The comparator M2 was constructed as a generic flexible two-state controller, and an explicit parameter embedding reproduces the M3 local transfer within numerical precision. This is a model-specific nesting certificate, not a claim that unrestricted neuronal latent-state models encompass every spatial SMM realization. The scored frequencies were 1–40 Hz, outside the most sensitive frequency regime of the isolated slow ionic pole. Consequently, neither the glial spatial geometry nor its most characteristic infraslow contribution was directly probed by this EEG comparison.

This yields a substantive modeling conclusion: there is no logical route from the failure of a local transfer constraint under one observation operator to the absence of a distinct spatial physiological controller. Equally, the failure cannot be renamed a success. The experiment tested what its executable represented, which was narrower than the defining class-level mechanism.

**2.7 Human resting EEG: the local constrained predictor generalized worse**

The EEG study reused the openly shared Dortmund Vital Study resting-state recordings (OpenNeuro ds005385, version 1.0.3) (Getzmann et al. 2024). The prespecified design assigned 565 subjects to the held-out comparison. Prespecified quality control excluded 27 participants, and a separately documented structural eligibility assessment excluded three more, leaving 535 included participants. A two-direction within-record split fitted each model on one chronological half and scored on the other, then reversed halves. Empirical cross-spectral matrices in the 1–40 Hz range were projected through the same fixed 20-dimensional observation basis and scored

using the same multivariate spectral likelihood. The comparator was M2, a generic two-state filter with the local M3 transfer family as an executable special case.

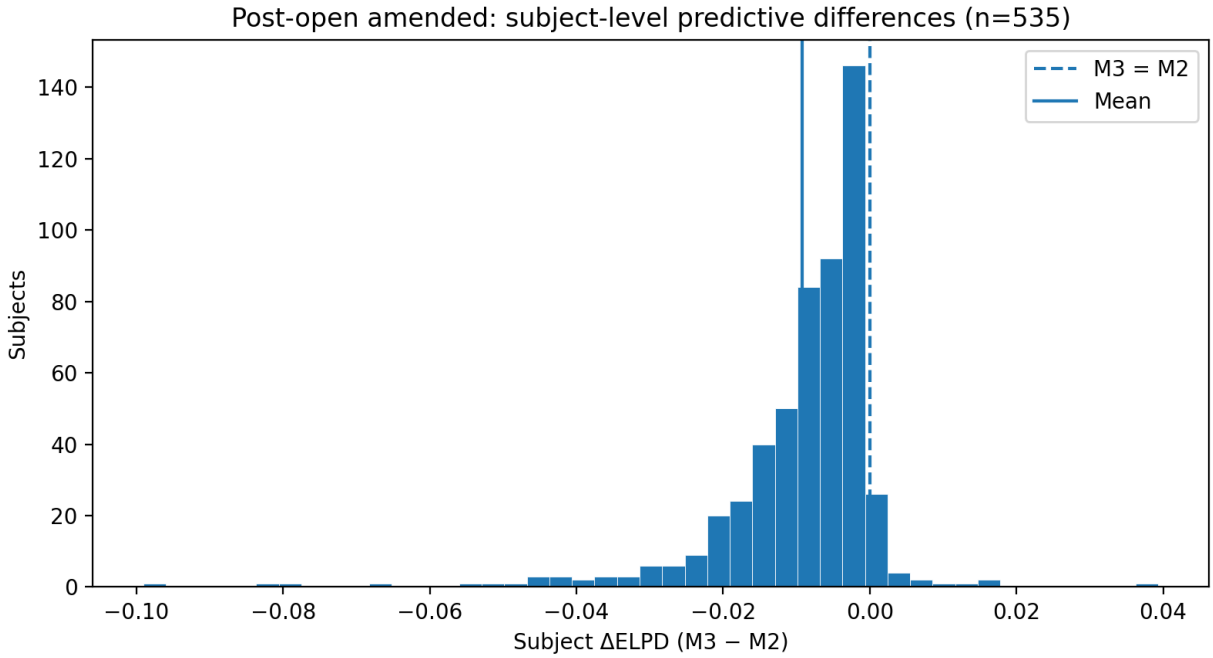


**Fig. 4** Participant-level held-out contrast for the amended EEG comparison

The frozen primary execution, run 37752719639, had integrity/execution failures and was **NOT EVALUABLE**. It was not converted to a valid confirmatory result. A separately logged repair and assembly produced a **POST_OPEN_AMENDED**, same-cohort descriptive and inferential completion on 8–11 October 2026, with final assembly run 38134531967. The mean participant-level contrast was $\overline{\Delta} = \mathrm{ELPD}(M3) - \mathrm{ELPD}(M2) = -0.00917841$ in the frozen normalized scoring convention, with median -0.00651430 and across-participant SD 0.01135554. A 10,000-resample participant bootstrap gave a 95% percentile interval [-0.01015793, -0.00823401]. M3 performed better than M2 in 24/535 participants (4.49%). The one-sided 100,000-sign-flip test of M3 superiority yielded $p = 1.0$. The direction of the result is unfavorable to the local ionic predictor and to the prespecified M3 predictive-superiority hypothesis.

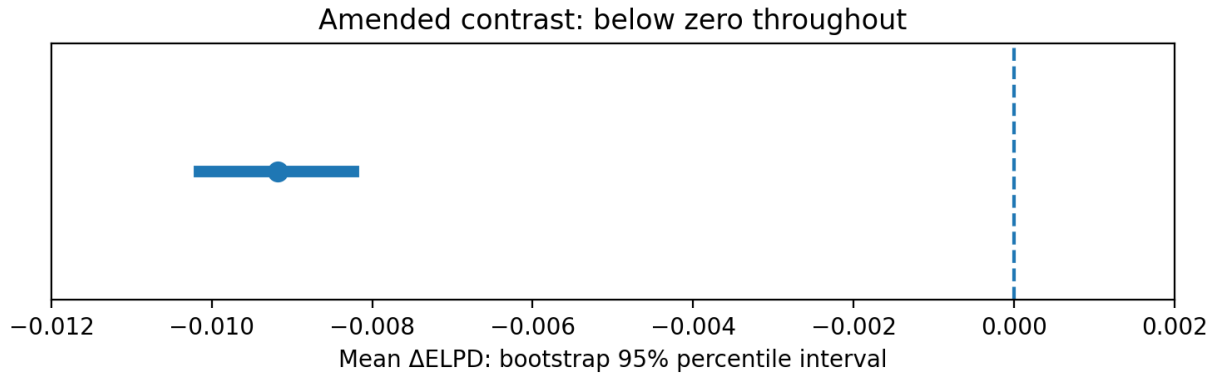


**Fig. 5** Bootstrap distribution of the same amended M3-minus-M2 mean, not an untouched confirmatory result

For numerical context, the participant-level mean M2 held-out score is 540.7356 with between-participant SD 12.0507, compared with a mean paired M3-minus-M2 difference of -0.0091784. The mean difference is small in these normalized score units even though its sign favors M2 in 511/535 participants. Expressing that difference as a percentage of the positive absolute M2 score would be misleading: the absolute log-score origin depends on additive likelihood constants and normalization, unlike the paired model difference. The sample size makes the mean signed contrast precise within the declared resampling procedure; its magnitude does not measure a physiological potassium effect, nor establish practical predictive equivalence. M0 (neuron-only) and M1 (generic one-state control) were specified in the prespecified model hierarchy, but the available 535-person amended *subject-level result artifact* reports only M2 and M3. M0/M1 comparative scores cannot be inferred from that file; their absence limits the interpretation of which generic slow mechanisms the data favor. The model-specific conclusion is that constraining the tested local two-state feedback to the proposed potassium parameters gave worse held-out within-record spectral prediction than allowing M2 the corresponding generic flexibility. It does not specify which of physiological mismatch, unmodeled non-glial

slow processes, template forward-model limitations or other estimation effects caused the difference. It also contains no test of $D_g$ because that parameter was absent from the executable.

### 2.8 Microscopic model checks and the limits of calibration

The biophysical reference construction includes membrane-current bookkeeping, extracellular–astroglial electrochemical reductions, a six-ion zero-flow reference system and microscopic impulse-response calculations. Reproducibility checks address resting-state flux relations and reduced linear pulse responses. A finite-volume implementation of the nonlinear six-ion R1 zero-flow equations produced 31-cell central extracellular potassium peaks of 0.13705955 and 0.27776327 mM for the two specified inputs. The latter rounds to 0.278 rather than the reported three-decimal reference of 0.277 mM; discretization differences across tested grids are of order one percent. These computations do not reproduce the full six-ion FEniCS electro-chemo-mechanical or R2 fluid-flow solver and do not independently calibrate the potassium parameters used in EEG-M3. The numerical evidence therefore establishes bounded checks of the reduction, not comprehensive physiological calibration (Online Resource 4).

The microscopic calculations constrain the derivation and numerical behavior of the ionic reduction, but do not identify a unique parameter set from extracellular recordings. A held-out reduced-mode check exceeded its nominal 10% normalized root-mean-square error limit, returning 10.47%. That failed threshold is reported in the source audit and cannot be counted as a successful validation of the local model.

## 3 Discussion

### 3.1 The decisive object is a stimulus-dependent response geometry

Astroglial spatial buffering is established physiology (Kofuji and Newman 2004; Orkand et al. 1966), and connexin manipulations show that glial network coupling can influence potassium

handling (Pannasch et al. 2011; Wallraff et al. 2006). The contribution of this model is the explicit dependence of neuronal response geometry on transport and stimulus mode, the persistence of that dependence under tested neuronal input routes and lateral coupling, and its exact absence from the local EEG observation model used for the reported comparison. These results identify a model-specific transport sensitivity rather than a newly discovered physiological buffering process.

The SMM architecture treats slow glial control as a physiological influence on neuronal dynamics, not as an additional direct electromagnetic source of scalp EEG (Ballús 2024; Ballús Santacana 2026). In the ionic realization, glial transport redistributes neuronal responses to focal forcing while leaving an exactly uniform mode insensitive in the homogeneous linear model. Neuronal connectivity and glial transport therefore specify distinct geometries, and the spatial structure of the perturbation is essential to identifying their effects. No claim about particular calcium-wave speeds or intrinsic ionic delta/theta oscillations follows from this result.

The positive spatial result is mathematically modest but conceptually important. It provides a quantitative link from a separately specified glial spatial operator through a local physiological state and into neuronal firing variables. It does not demonstrate that the brain uses that value of $D_g$ or produces the simulated response magnitude. Its prospective predictive content is the *stimulus-pattern-by-glial-coupling interaction* defined in Eq (7): under suitable stable operating regimes, a coupling manipulation should differentially alter neuronal response geometry after spatially patterned versus near-uniform forcing, once neuronal connectivity and alternative physiological pathways are constrained. The source-normalized 20-s adjacent/central ratio in Fig. 2 illustrates the model response geometry; it is neither the primary proposed experimental estimand nor an empirical effect-size commitment for all preparations.

The associated modal result separates two propositions often conflated in multiscale models. A local glial feedback pathway can exist and have a slow pole without expressing a dependence on glial connectivity. Conversely, a spatially extended coupling term can alter the local neuronal state while a chosen observation operator is insensitive to it. These are statements about different maps: physical parameters to local causal dynamics, and physical parameters to measured distributions. A model may be adequate under the first and uninformative under the second. SMM must therefore be tested through mechanisms that survive the planned observation and perturbation, rather than via biological labels assigned to latent spectral filters.

### 3.2 The negative EEG comparison is adverse evidence, not a refutation by proxy

The held-out EEG results provide adverse evidence for the tested constrained local potassium predictor: the amended participant-level comparison favored the generic two-state controller. The model difference should not be described as predictive equivalence. However, this inference is restricted by the implemented observation model: its likelihood depends on local ionic filtering but not on glial spatial transport or on a focal-versus-uniform response contrast. Equations (5) and (6) distinguish the spatial transport sensitivity from the spectral projection actually tested. The adverse result therefore constrains the local predictor without directly estimating the glial transport parameter.

Two independent limitations further narrow the biological interpretation. The recorded 1–40 Hz band did not contain the isolated approximately 0.018-Hz ionic corner; moreover, the EEG forward model used a generic template leadfield and a fixed low-dimensional sensor projection. Neither limitation proves that real infraslow recordings would detect astroglia. But both establish that the reported failure does not answer the strongest biologically specific question the SMM

model poses. An independent infraslow or perturbational experiment must be designed without retuning the held-out cohort, and its success rule must be locked before testing.

### 3.3 Competing explanations and what would distinguish them

Existing glia–neuron and neural-field models provide biologically credible alternative explanations for slow neuronal dynamics (Ali et al. 2025; Amiri et al. 2012; Cressman et al. 2009; Gong et al. 2024; Halnes et al. 2013; Lenk et al. 2020; Moran et al. 2007; Moran et al. 2009; Olenin et al. 2023; Robinson et al. 2001; Stasenko et al. 2025; Sætra et al. 2021; Sætra et al. 2023; Ullah et al. 2009). A generic local neuronal controller can emulate the zero-mode potassium transfer; a spatial neuronal network can generate interpatch propagation; and vascular or neuromodulatory processes can generate slow excitability changes without a distinct glial transport pathway. Accordingly, empirical discrimination cannot rely solely on nonlocal response patterns or on assigning a glial label to an unobserved latent state. Competing models must be compared under independently constrained physiological and spatial operators.

The proposed discriminating design requires a matched comparison across two stimulation patterns (focal and approximately uniform) and two independently characterized glial-coupling conditions. It should combine electrophysiology with extracellular potassium and astroglial-state measurements, while constraining changes to neuronal connectivity, extracellular diffusion, baseline excitability and nonspecific interventions. Define the primary *site-resolved experimental interaction* as

$$C_j(t;u) = Y_j(t \mid u, g_H) - Y_j(t \mid u, g_L),$$
$$\mathcal{I}_j(t) = C_j(t;u_F) - C_j(t;u_U).$$

where $C_j$ is the within-stimulus glial-coupling contrast and $Y_j$ is the baseline-corrected neuronal response at recording site $j$, $u_F$ and $u_U$ are focal and independently verified approximately uniform perturbations, and $g_H$ and $g_L$ denote measured high- and low-glial-coupling conditions.

Input dose, baseline potassium and response gain must be measured or matched; the two stimulus routes cannot simply be assumed to deliver identical physiological doses. In the homogeneous computational counterfactual $g_H$ and $g_L$ correspond to the reference $D_g$ and $D_g = 0$; the uniform-input bracket is exactly zero because $L_g\mathbf{1} = 0$. Thus the modeled interaction equals the within-route focal transport contrast, **not an independent simulated test**. In biological preparations, the second bracket need not be zero, and a connexin manipulation does not uniquely set the scalar $D_g$.

The adjacent/central response ratio $\mathcal{R}(t) = \delta r_E(\text{adjacent}, t)/\delta r_E(\text{center}, t)$ remains a useful illustration of geometry, but it is secondary to $\mathcal{I}_j(t)$: neuronal lateral propagation can raise both baseline responses and sharply dilute the ratio's relative sensitivity without eliminating the absolute transport-dependent increment. Under the focal neuron-derived potassium source in the present linear model, the adjacent-site interaction at 20 s is $0.001751$, $0.001625$ and $0.001414$ source-normalized units for $\gamma_N = 0$, 10 and 30 $s^{-1}$. Under direct neuronal-voltage drive the corresponding values are $0.000204$, $0.000176$ and $0.000132$, but the latter is only about 0.49% of its no-transport adjacent response. Magnitudes across different drive types are not dose-calibrated and must not be compared as equivalent biological effect sizes (Online Resource 6).

A concrete preparation is a hippocampal slice comparison of focal $K^+$ iontophoresis (or physiologically evoked focal neuronal potassium release) with approximately homogeneous bath $K^+$ elevation, accompanied by potassium-selective electrodes at several distances, multi-site neuronal recordings and a direct measure of astrocytic coupling. Comparisons could use conditional astrocytic Cx43 deletion combined with Cx30 deficiency and matched controls, following precedents in Wallraff et al. (Wallraff et al. 2006) and Pannasch et al. (Pannasch et al. 2011). These studies support feasibility, not selectivity: connexin changes can also alter

glutamate clearance, extracellular-space volume, baseline synaptic drive and network excitability. Bath application approximates a uniform mode only if its spatial concentration profile is verified. A matched neuronal-only or alternative-physiology model must predict *both* spatial input conditions with common, independently constrained parameters. The falsifiable target is an out-of-sample spatial interaction attributable to a specified glial transport pathway after relevant competing changes have been measured, not the observation of nonlocal neuronal spread alone.

The broader class must also be stated in a falsifiable bounded form. If coupling strengths can approach zero, an arbitrarily small glial effect cannot be excluded by any finite noisy experiment with useful power. Genuine empirical competition requires a parameter region justified by independent physiology, a perturbation range, a measured response operator, a minimum biologically meaningful effect size and a prospective decision rule. The analytic mode sensitivity provides the object to bound; the existing EEG outcome cannot retroactively determine its threshold.

### 3.4 Relation to prior physiological models and alternative field mechanisms

A damped glial-field equation describes an alternative dynamical mechanism to the passive SMM-K potassium block. The real negative ionic poles of the latter do not yield sustained traveling delta/theta oscillations. An underdamped field instead requires restoring or regenerative dynamics with independently specified physiological coupling, propagation scales and boundary conditions. Phenomenological phase-gradient and spectral fits reported in the SMM preprint (Ballús 2024) do not by themselves identify an astroglial propagation speed or establish that such wave modes generate measured human rhythms. The associated numerical and dimensional

constraints are documented in Online Resources 2 and 5; they are not treated as independent confirmation of the potassium-based spatial prediction.

A published conceptual account of glial syncytial control fields and their possible role in low-frequency neuronal organization supplies part of the physiological motivation (Ballús Santacana 2026). The results established here are distinct: an operational coupled-model class, an explicit potassium-mediated dynamical realization, spatial perturbation and mode sensitivities, and the bounded interpretation of a held-out EEG comparison. The prior article is credited as conceptual work rather than counted as independent quantitative validation. Publication overlap and the evidential status of preprint simulations are specified in Online Resource 2.

The causal hypothesis is therefore conditional and empirically testable: with neuronal connectivity and local physiology constrained, a change in glial transport should interact with the spatial pattern of input to alter neuronal response geometry. In contrast, the local EEG predictor retains no parameter representing this spatial transport, so its negative comparison addresses a different, narrower statistical model. A prospective test requires physiological estimates of coupling, spatially resolved interventions and an independently specified comparison model.

### 3.5 Limitations

The spatial prediction arises from a seven-domain linearization of a near-equilibrium SMM-K parameter set; it is not an in-vivo demonstration of glial causal control. The model uses symmetric local Laplacians, positive scalar coefficients and homogeneous patches. Heterogeneous transport, nonlinear pumps, electrodiffusive boundaries and glial calcium dynamics could alter or eliminate the calculated directional effect. Direct forcing of the astroglial state is an idealization; additional calculations with neuron-derived potassium input and direct neuronal excitation test two alternative routes but do not represent calibrated tissue interventions.

Phenomenological neuronal lateral coupling is not independently fitted connectivity. Under the strongest tested lateral coupling, the direct-excitation transport effect is less than 1% of the adjacent no-transport response, and its presence in exact arithmetic does not establish experimental detectability. A biological effect-size claim requires independently calibrated inputs, transport conditions and observations.

The EEG comparison uses derived participant-level scores rather than an independently repeated fit of all 535 raw EEG recordings. Forward and statistical operators and aggregate calculations were checked, but complete participant-level optimization paths were not rerun. The post-open amendment limits confirmatory interpretation, while the untouched frozen primary is not evaluable. Within-participant training and testing used distinct chronological epochs but shared full-recording preprocessing, not independent raw-signal pipelines. The observation model retained only a local two-pole potassium transfer, template source projection and a frequency range poorly matched to the isolated slow ionic corner. The M2–M3 score difference therefore does not identify a unique physiological cause. The full nonlinear six-ion FEniCS/R2 flow solver was also not independently reproduced. These restrictions limit the biological interpretation of both the spatial and empirical results.

## 4 Materials and methods

### 4.1 Definition of the causal model class

The general system in Eq (1) was formulated to separate a neuronal population generator $x$ and anatomical neuronal matrix $W_N$ from glial/extracellular physiological states $z$ and a local glial transport or interaction matrix $L_g$. SMM membership in this operational formalization requires (i) a physiologically interpreted glial state, (ii) a glial coupling geometry not reducible by definition to $W_N$, (iii) a bidirectional neuronal–glial–neuronal causal path, (iv) a specified

timescale separation relative to selected neuronal variables, (v) principal neuronal generation of EEG/MEG and (vi) a possible glial-transport dependence of neuronal states under a spatially structured intervention. These conditions were formalized after the EEG result; they are not presented as predeclared experimental constraints. The biological class contains several potential channels, but the computational study tests only SMM-K.

### 4.2 Local and spatial potassium model

Equation (2) specifies potassium exchange and clearance in the two-compartment ionic reduction. Positive parameters used by the frozen EEG implementation were $\phi_e = 0.2$, $\phi_a = 0.4$, $\kappa_e = 2.01315923$, $\kappa_a = 0.48318016$ and $\kappa_N = 0.232$, with the time and source conventions of the fixed executable. The neuronal population portion comprised an excitatory–inhibitory QIF-derived linearization with three state-pairs and potassium feedback to neuronal excitability; the exact matrix entries and units are in the source script audit_frozen_eeg_m3_local.py. SMM-K is not a parameter-free model; its local coefficients are inherited from a specific reduction and are not asserted to be independently estimated in the EEG cohort.

For the Lyapunov statement, $J_N = 0$ and $L_e, L_g$ are symmetric nonnegative graph Laplacians in matched exchange coordinates. Differentiating the stated positive-definite $V$ yields Eq (3). The sum of squares is strictly negative for any nonzero state because $\kappa_N > 0$, $\kappa_a > 0$ and all other terms are nonnegative. The isolated ionic subsystem is therefore globally exponentially stable. When $L_e, L_g$ share a mode, the associated two-dimensional ionic matrix has real negative eigenvalues: its characteristic discriminant is the sum of a square and $4\kappa_e\kappa_a/(\phi_e\phi_a)$. General noncommuting transport does not invalidate the quadratic argument, although it prevents this simple simultaneous modal decomposition.

### 4.3 Spatial input and causal counterfactual

Seven local domains were connected as a path with open endpoints, Laplacian scaled by $h^{-2}$ and $h = 150\,\mu$m. The eight-dimensional frozen local Jacobian $A_8$ was placed on each diagonal block. Extracellular diffusion was added to potassium coordinate 6, and glial transport to astroglial coordinate 7, producing a stable $56 \times 56$ matrix $A(D_g)$. A constant source-normalized input $Bu$ was placed in the center astroglial coordinate. The response of the linear system over duration $t$ was evaluated exactly up to floating-point error via

$$q(t) = A(D_g)^{-1}\left(e^{A(D_g)t} - I\right)Bu,$$

and the excitatory neuronal-rate components were read from coordinates 0, 8, …, 48. The matched comparator held all parameters fixed except $D_g = 0$. Additional trials injected identical inputs into all seven astroglial coordinates, which preserve the uniform eigenspace. Numerical stability was checked for both conditions. Values at 0.1, 1, 3, 8 and 20 s and the transport-coefficient sweep are supplied as a machine-readable JSON and executable script. This calculation concerns the stated linearized spatial counterfactual and does not reproduce the nonlinear electrodiffusive system analyzed in Online Resource 4.

### 4.4 Retrospective sensitivity calculations with neuronal input and lateral coupling

The reference center-patch input acted on astroglial coordinate $a_i$ with unit drive $1/\phi_a$. Two alternate constant focal inputs were introduced separately without changing the local QIF/ion Jacobian: (i) a neuronal potassium-release proxy with drive $1/\phi_e$ into extracellular potassium coordinate $k_i$, and (ii) an excitatory neuronal voltage input with drive $1/\tau_E$ into $V_{E,i}$. The latter excites the specified rate-to-potassium pathway through the nonzero $J_{RE}\, r_E/\phi_e$ term already present in the frozen local model. The source-normalization conventions differ between these

drives, so magnitudes are not compared as equal delivered biological doses; only *within-source* $D_g$ contrasts are meaningful.

For a seven-site path with unscaled graph Laplacian $L$, a phenomenological neuronal lateral coupling was introduced as $\dot{\mathbf{r}}_E \mapsto \dot{\mathbf{r}}_E - \gamma_N L\mathbf{r}_E$. This is distinct from the glial term $-\left(D_g/\phi_a h^2\right)L\mathbf{a}$, and from the long-range EEG neuronal matrix $W_N$. The parameter $\gamma_N$ was swept over 0, 0.3, 1, 3, 10, 30 $s^{-1}$; a secondary rate-to-voltage diffusion $-(\gamma_N/\tau_E)L\mathbf{r}_E$ was tested at the dimensionless coefficients 0, 0.001, 0.003, 0.01, and 0.03. For each input, $D_g$ was compared at zero and the reference value, leaving $\gamma_N$, $D_e$, local rate coupling and the observation coordinates unchanged. All reported linearizations retained negative-real-part eigenvalues. Source-normalized responses were evaluated at 3, 8 and 20 s through the exact linear step-response integral; a simultaneous-eigenmode method was cross-checked against the explicit 56-state matrix exponential, with maximum absolute discrepancy $1.7 \times 10^{-13}$. Uniform-input invariance was rechecked. These are retrospective *robustness tests*, not a prospective experiment, and do not calibrate the neuronal-coupling coefficients. Their full executable methods, JSON output and plotted comparisons are in Online Resource 6, Online Resource 3, and Online Resource 7.

**4.5 Mode-level transfer and sensitivity**

When the two Laplacians commute (as in the seven-site shared path), the $K$ balance can be restricted to a common spatial eigenmode. Algebraic inversion of its $2 \times 2$ frequency-domain matrix gives Eq (4). Differentiating the rational function yields Eq (5). Analytic derivatives were compared against centered finite differences in the provided script at $f = 0,0.01,0.018,0.05,0.1,1,8,40$ Hz for the uniform and selected nonuniform modes. The script includes stability, homogeneity and derivative checks. The assertion is not that any frequency dependence uniquely establishes glial identity; it is that this specified physiological mechanism

creates a transport-sensitive mode transfer that disappears if one retains only the zero spatial mode.

### 4.6 Frozen EEG observation model and comparator

The EEG executable used 68 DK cortical regions and a normalized anatomical neuronal matrix with delays approximated from Euclidean region-centroid distances. A template regional leadfield $L \in \mathbb{R}^{64\times 68}$ and 20-component orthonormal projection $U_{20}$ provided the common observation operator. Model spectra had the form

$$S_{y,m}(f) = a^2(p_E(L_{20}H_E)(L_{20}H_E)^\dagger + (1-p_E)(L_{20}H_I)(L_{20}H_I)^\dagger) + \sigma_0 I_{20},$$
$$L_{20} = U_{20}^\top L.$$

The M3 local filter is Eq (4) at $\mu_e = \mu_g = 0$; no spatial glial operator is an input to the frozen program. M2 was the flexible two-state filter comparator, M1 a distinct generic one-state controller, and M0 the neuron-only baseline. The available held-out participant-level comparison is M3 versus M2, as specified in the frozen protocol; it does not report M3 versus M1 or M3 versus the neuron-only M0 baseline. An exact pair of partial fractions embeds the M3 uniform filter in M2 within its tested bounds. The full chain through neuronal network, leadfield and spectral score was replayed at frozen frequencies by the source code audit; the reproduction package records exact code identifiers and tolerances.

### 4.7 EEG cohort, scoring and inferential provenance

Raw source: OpenNeuro ds005385 v1.0.3, Dortmund Vital Study, resting eyes-closed pre-task session (Getzmann et al. 2024), with publicly documented de-identified data. A common processing sequence used MNE, PREP and ICLabel software (Bigdely-Shamlo et al. 2015; Gramfort et al. 2014; Pion-Tonachini et al. 2019; Thomson 1982), full-recording artifact QC, resampling to 250 Hz, 0.5–45 Hz analysis filtering, four-second epochs, and at least 30 retained epochs per participant. The fixed data split compared successive chronological halves A and B in

both fit/score directions. Multivariate CSDs at 1–40 Hz used DPSS multitapers (time-bandwidth NW=3, Kmax=5) (Thomson 1982) and a shared 20-component projection. The normalized complex Whittle-style score was, up to constants common to both models,

$$\ell_m = -\sum_f \nu_f \left(\log\det S_m(f) + \mathrm{tr}\{S_m(f)^{-1}\hat{S}(f)\}\right), \qquad \Delta_i = L_{M3,i} - L_{M2,i}.$$

Each $L_{m,i}$ averaged the held-out score for A-fitted/B-scored and B-fitted/A-scored predictions. The frozen success condition required both a positive lower bound for the participant-bootstrap confidence interval of the mean $\Delta$ and a one-sided sign-flip $p < 0.05$ favoring M3. The frozen primary run 37752719639 was **NOT EVALUABLE** owing to execution/provenance faults; it was never converted into a confirmatory outcome. The explicitly **POST_OPEN_AMENDED** run record restored subject 075 after a channel-provenance repair, separated structural ineligibility of subjects 206, 230 and 425, and assembled final artifacts without changing model definitions, cohort membership rules or endpoints. The recorded amended fit and final assembly provenance comprises runs 37787000597, 37968393249 and 38134531967. Aggregate and participant-resampling computations were independently rerun from archived CSV/JSON. Their agreement does not replace a full independent refitting of all raw EEG recordings.

### 4.8 Microscopic numerical checks and the scope of evidence

The biophysical reference calculations comprise zero-flow six-ion balance, nonlinear and linear spatial discretizations, and ionic pulse responses. Numerical checks verified resting flux bookkeeping and selected linear ionic responses. A finite-volume R1 implementation supplies a bounded numerical comparison across grid resolutions, but the high-fidelity FEniCS six-ion system, R2 advective flow computations and source-level cellular calibration were not independently reproduced. The reported outcomes are not used to assert quantitative validation against physiological tissue measurements. The code archive contains executable checks,

parameter records and run-provenance logs, while Online Resources 2, 4 and 5 distinguish the empirical status of the conceptual, ionic and alternative field realizations.

### 4.9 Generative AI assistance

**Generative AI assistance.** OpenAI ChatGPT (GPT-5.6 and GPT-6) was used to assist with language and structural editing, literature searches, code development, and computational checks. AI-assisted material was reviewed and revised by the author, who takes full responsibility for the content, accuracy, and conclusions of the manuscript.

## 5 Conclusion

The Syncytial Mesh Model specifies a physiological control geometry that interacts with neuronal dynamics without treating astrocytes as the principal electrical source of EEG. In its potassium realization, neuronal responses to a focal perturbation depend on glial transport, whereas the exactly uniform mode of the homogeneous linearized system is transport-insensitive. The resulting stimulus-pattern dependence has an explicit transfer-function representation and defines a candidate spatial intervention contrast. The available human EEG comparison instead tested a local ionic transfer without the glial spatial operator and, in a post-open amended analysis, favored a generic two-state controller; the frozen primary was not evaluable. The EEG result therefore constrains the local predictor but does not test transport sensitivity. Distinguishing the proposed biological pathway from neuronal propagation and other slow-control mechanisms requires independently calibrated, spatially resolved interventions and prospective model comparisons.

## Statements and Declarations

Data and code availability. Original EEG recordings are publicly available from OpenNeuro ds005385 v1.0.3, DOI: 10.18112/openneuro.ds005385.v1.0.3. The subject-level amended scores,

spatial-model output, exact parameters, reproducibility scripts and source numerical audit accompany this article as machine-readable Online Resource 3 (ESM_3_Data_and_Code.zip). The SMM code repository is publicly accessible at https://github.com/ipsissima/SMM and is MIT-licensed (https://github.com/ipsissima/SMM/blob/main/LICENSE). The frozen EEG implementation is pinned to scientific base commit 20fab272edf33d2513470c60ac9398754535cacb. The independent reference solver source is at https://github.com/martejulie/fluid-flow-in-astrocyte-networks, commit 99bfe1671d9c5735333fa24c2406aa32bde010fc. The manuscript-specific code/data archive is supplied with this submission; no separate permanent public accession or reuse licence for that archive is claimed.

**Ethics approval and consent.** No new human participants were recruited or contacted. The human analysis reuses public, de-identified Dortmund Vital Study EEG recordings. Original ethics and consent statements are those of the dataset investigators (Getzmann et al. 2024); this analysis does not assert a new, undocumented approval or consent exemption.

Related publications and preprints. The three-layer SMM proposal and alternative field formulations appeared in the Brain-Mesh / Syncytial Mesh preprints (Ballús 2024; arXiv:2412.12106; bioRxiv:2024.11.22.624908). The published conceptual account of glial syncytial control fields (Ballús Santacana 2026) is separately credited. Neither publication is presented as independent numerical or empirical validation of the potassium realization; the precise relationship of the results is documented in Online Resource 2.

**References**

Ali OBK, Vidal A, Grova C, Benali H (2025) Dialogue mechanisms between astrocytic and neuronal networks: a whole-brain modelling approach. PLoS Comput Biol 21:e1012683. https://doi.org/10.1371/journal.pcbi.1012683

Amiri M, Bahrami F, Janahmadi M (2012) On the role of astrocytes in epilepsy: a functional modeling approach. Neurosci Res 72:172–180. https://doi.org/10.1016/j.neures.2011.11.006

Ballús A (2024) The Brain-Mesh Model: A Unified Framework for Neural Synchrony, Plasticity, and Coherence; later revised as The Syncytial Mesh Model [preprint]. arXiv:2412.12106. https://arxiv.org/abs/2412.12106. Related bioRxiv preprint: https://doi.org/10.1101/2024.11.22.624908

Ballús Santacana A (2026) Glial syncytial control fields and the low-frequency resonome of the human brain. Front Hum Neurosci 20:1896291. https://doi.org/10.3389/fnhum.2026.1896291

Bigdely-Shamlo N, Mullen T, Kothe C, Su KM, Robbins KA (2015) The PREP pipeline: standardized preprocessing for large-scale EEG analysis. Front Neuroinform 9:16. https://doi.org/10.3389/fninf.2015.00016

Clasadonte J, Scemes E, Wang Z, Boison D, Haydon PG (2017) Connexin 43-mediated astroglial metabolic networks contribute to the regulation of the sleep-wake cycle. Neuron 95:1365–1380.e5. https://doi.org/10.1016/j.neuron.2017.08.022

Cressman JR Jr, Ullah G, Ziburkus J, Schiff SJ, Barreto E (2009) The influence of sodium and potassium dynamics on excitability, seizures, and the stability of persistent states: I. Single neuron dynamics. J Comput Neurosci 26:159–170. https://doi.org/10.1007/s10827-008-0132-4

Donoghue T, Haller M, Peterson EJ, Varma P, Sebastian P, Gao R, et al (2020) Parameterizing neural power spectra into periodic and aperiodic components. Nat Neurosci 23:1655–1665. https://doi.org/10.1038/s41593-020-00744-x

Getzmann S, Gajewski PD, Schneider D, Wascher E (2024) Resting-state EEG data before and after cognitive activity across the adult lifespan and a 5-year follow-up. Sci Data 11:988. https://doi.org/10.1038/s41597-024-03797-w

Gong L, Pasqualetti F, Papouin T, Ching S (2024) Astrocytes as a mechanism for contextually-guided network dynamics and function. PLoS Comput Biol 20:e1012186. https://doi.org/10.1371/journal.pcbi.1012186

Gramfort A, Luessi M, Larson E, Engemann DA, Strohmeier D, Brodbeck C, et al (2014) MNE software for processing MEG and EEG data. NeuroImage 86:446–460. https://doi.org/10.1016/j.neuroimage.2013.10.027

Halnes G, Østby I, Pettersen KH, Omholt SW, Einevoll GT (2013) Electrodiffusive model for astrocytic and neuronal ion concentration dynamics. PLoS Comput Biol 9:e1003386. https://doi.org/10.1371/journal.pcbi.1003386

Kofuji P, Newman EA (2004) Potassium buffering in the central nervous system. Neuroscience 129(4):1045–1056. https://doi.org/10.1016/j.neuroscience.2004.06.008

Lenk K, Satuvuori E, Lallouette J, Ladron-de-Guevara A, Berry H, Hyttinen JAK (2020) A computational model of interactions between neuronal and astrocytic networks: the role of astrocytes in the stability of the neuronal firing rate. Front Comput Neurosci 13:92. https://doi.org/10.3389/fncom.2019.00092

Montbrió E, Pazó D, Roxin A (2015) Macroscopic description for networks of spiking neurons. Phys Rev X 5:021028. https://doi.org/10.1103/PhysRevX.5.021028

Moran RJ, Kiebel SJ, Stephan KE, Reilly RB, Daunizeau J, Friston KJ (2007) A neural mass model of spectral responses in electrophysiology. NeuroImage 37:706–720. https://doi.org/10.1016/j.neuroimage.2007.05.032

Moran RJ, Stephan KE, Seidenbecher T, Pape HC, Dolan RJ, Friston KJ (2009) Dynamic causal models of steady-state responses. NeuroImage 44:796–811. https://doi.org/10.1016/j.neuroimage.2008.09.048

Olenin SM, Levanova TA, Stasenko SV (2023) Dynamics in the reduced mean-field model of neuron--glial interaction. Mathematics 11:2143. https://doi.org/10.3390/math11092143

Orkand RK, Nicholls JG, Kuffler SW (1966) Effect of nerve impulses on the membrane potential of glial cells in the central nervous system of amphibia. J Neurophysiol 29:788–806. https://doi.org/10.1152/jn.1966.29.4.788

Pannasch U, Vargová L, Reingruber J, Ezan P, Holcman D, Giaume C, et al (2011) Astroglial networks scale synaptic activity and plasticity. Proc Natl Acad Sci USA 108:8467–8472. https://doi.org/10.1073/pnas.1016650108

Pion-Tonachini L, Kreutz-Delgado K, Makeig S (2019) ICLabel: an automated electroencephalographic independent component classifier, dataset, and website. NeuroImage 198:181–197. https://doi.org/10.1016/j.neuroimage.2019.05.026

Poskanzer KE, Yuste R (2016) Astrocytes regulate cortical state switching in vivo. Proc Natl Acad Sci U S A 113:E2675–E2684. https://doi.org/10.1073/pnas.1520759113

Robinson PA, Loxley PN, O'Connor SC, Rennie CJ (2001) Modal analysis of corticothalamic dynamics, electroencephalographic spectra, and evoked potentials. Phys Rev E 63:041909. https://doi.org/10.1103/PhysRevE.63.041909

Sætra MJ, Einevoll GT, Halnes G (2021) An electrodiffusive neuron-extracellular-glia model for exploring the genesis of slow potentials in the brain. PLoS Comput Biol 17:e1008143. https://doi.org/10.1371/journal.pcbi.1008143

Sætra MJ, Ellingsrud AJ, Rognes ME (2023) Neural activity induces strongly coupled electro-chemo-mechanical interactions and fluid flow in astrocyte networks and extracellular space: a computational study. PLoS Comput Biol 19:e1010996. https://doi.org/10.1371/journal.pcbi.1010996

Stasenko SV, Olenin SM, Grines EA, Levanova TA (2025) Firing rate model for brain rhythms controlled by astrocytes. Eur Phys J Spec Top 234:2045–2055. https://doi.org/10.1140/epjs/s11734-024-01336-7

Thomson DJ (1982) Spectrum estimation and harmonic analysis. Proc IEEE 70:1055–1096. https://doi.org/10.1109/PROC.1982.12433

Ullah G, Cressman JR Jr, Barreto E, Schiff SJ (2009) The influence of sodium and potassium dynamics on excitability, seizures, and the stability of persistent states: II. Network and glial dynamics. J Comput Neurosci 26:171–183. https://doi.org/10.1007/s10827-008-0130-6

Wallraff A, Köhling R, Heinemann U, Theis M, Willecke K, Steinhäuser C (2006) The impact of astrocytic gap junctional coupling on potassium buffering in the hippocampus. J Neurosci 26:5438–5447. https://doi.org/10.1523/JNEUROSCI.0037-06.2006

**Supplementary Information: Online Resources**

Online Resource 1 (ESM_1_Analytical_Proofs.pdf). Mathematical proofs, causal model conditions, modal transfer discrimination, and exact limits of the observation operator.

Online Resource 2 (ESM_2_Preprint_Lineage.pdf). Prior technical preprints, attribution to the published conceptual article, superseded simulation claims and publication overlap.

Online Resource 3 (ESM_3_Data_and_Code.zip). Reproducibility scripts, exact model constants, spatial response tables, numerical-check output, amended participant-level derived contrasts, and the prior audited verification bundle; includes full provenance notices.

Online Resource 4 (ESM_4_Microscopic_Reproducibility.pdf). Six-ion reference calculations, numerical reproducibility checks, limitations of the R1/R2 solver comparisons and the held-out reduced-mode threshold.

Online Resource 5 (ESM_5_Alternative_Realizations.pdf). Alternative neuronal, connectomic, damped-field and plasticity models, together with their physiological assumptions, parameter scales and evidence boundaries relative to SMM-K.

Online Resource 6 (ESM_6_Neuronal_Input_Robustness.pdf). Retrospective sensitivity calculations performed after the EEG outcome using neuron-derived potassium sources, direct neuronal excitation and lateral neuronal coupling; complete numerical output and computational conditions.

Online Resource 7 (ESM_7_Supplementary_Figure.pdf). Transport-dependent focal neuronal responses under neuron-derived potassium and direct neuronal-voltage inputs; the neighboring response interaction is shown alongside the descriptive ratio, using exact conditional model outputs at 20 s rather than experimentally calibrated activity.

## Supplementary Files

This is a list of supplementary files associated with this preprint. Click to download.

- ESM3Description.pdf
- ESM7SupplementaryFigure.pdf
- ESM2PreprintLineage.pdf
- ESM1AnalyticalProofs.pdf
- ESM6NeuronalInputRobustness.pdf
- ESM4MicroscopicReproducibility.pdf
- ESM5AlternativeRealizations.pdf
- ESM3DataandCode.zip